ELSEVIER

Journal of Atmospheric and Solar-Terrestrial Physics ▮ (▮▮▮▮) ▮▮▮–▮▮▮

Journal of ATMOSPHERIC AND SOLAR-TERRESTRIAL PHYSICS

www.elsevier.com/locate/jastp

Coupled model simulation of a Sun-to-Earth space weather event

Janet G. Luhmann[a], Stanley C. Solomon[b,*], Jon A. Linker[c], John G. Lyon[d], Zoran Mikic[c], Dusan Odstrcil[e], Wenbin Wang[b], Michael Wiltberger[b]

[a]*University of California, Berkeley, CA 94720, USA*
[b]*National Center for Atmospheric Research, Boulder, CO 80309, USA*
[c]*Science Applications International Corporation, San Diego, CA 92121, USA*
[d]*Dartmouth College, Hanover, NH 03755, USA*
[e]*University of Colorado, Boulder, CO 80309, USA*

Abstract

This paper describes the 3D simulation of a space weather event using the coupled model approach adopted by the Center for Integrated Space Weather Modeling (CISM). The simulation employs corona, solar wind, and magnetosphere MHD models, and an upper atmosphere/ionosphere fluid dynamic model, with interfaces that exchange parameters specifying each component of the connected solar terrestrial system. A hypothetical coronal mass ejection is launched from the Sun by a process emulating photospheric field changes such as are observed with solar magnetographs. The associated ejected magnetic flux rope propagates into a realistically structured solar wind, producing a leading interplanetary shock, sheath, and magnetic cloud. These reach 1 AU where the solar wind and interplanetary magnetic field parameters are used to drive the magnetosphere–ionosphere–thermosphere coupled model in the same manner as upstream in situ measurements. The simulated magnetosphere responds with a magnetic storm, producing enhanced convection and auroral energy inputs to the upper atmosphere/ionosphere. These results demonstrate the potential for future studies using a modular, systemic numerical modeling approach to space weather research and forecasting.

Keywords: Space weather; Modeling; Coronal mass ejections; Heliosphere; Magnetosphere–ionosphere coupling

1. Introduction

Comprehensive numerical modeling of tropospheric weather and climate have long inspired visions of system-wide space weather simulations (c.f., National Space Weather Program Council, 2000). Advances in both computational tools and knowledge of the variety of solar-terrestrial relationships are now producing the first steps toward realizing this goal. The Center for Integrated Space Weather Modeling (CISM), led by Boston University (Principal Investigator W.J. Hughes),

*Corresponding author. Tel.: +1-303-497-2179; fax: +1-303-497-1589.

E-mail addresses: jgluhman@cism.ssl.berkeley.edu (J.G. Luhmann), stans@ucar.edu (S.C. Solomon), jon.a.linker@saic.com (J.A. Linker), lyon@tinman.dartmouth.edu (J.G. Lyon), zoran.mikic@saic.com (Z. Mikic), dusan.odstrcil@noaa.gov (D. Odstrcil), wbwang@ucar.edu (W. Wang), wiltbemj@ucar.edu (M. Wiltberger).

1364-6826/$ - see front matter © 2004 Elsevier Ltd. All rights reserved.
doi:10.1016/j.jastp.2004.04.005

seeks to simulate the system by coupling state-of-the-art codes modeling the solar corona, solar wind, magnetosphere and upper atmosphere/ionosphere. In contrast, other efforts (e.g., Groth et al., 2000) are developing a single unified algorithmic framework. The CISM modular approach, illustrated by the flow chart in Fig. 1, requires that the physical interchanges and computational logistics of the component code couplings are a substantial and challenging part of the effort. In exchange, it holds the future prospect of a flexible choice of component codes and versions. This paper describes the first CISM simulation of the production of a three-dimensional coronal transient, its propagation through a structured solar wind, and its interaction with the Earth's magnetosphere, ionosphere, and thermosphere.

As seen in Fig. 1, the major code elements of the CISM coupled model are the magnetohydrodynamics around a sphere (MAS) coronal model developed by Linker et al. (1999), the ENLIL solar wind model developed by Odstrcil and Pizzo (1999), the Lyon–Fedder–Mobarry (LFM) magnetosphere model (Fedder and Lyon, 1995; Fedder et al., 1995; Lyon et al., this issue), and the thermosphere–ionosphere-nested-grid (TING) model describing the upper atmosphere and ionosphere

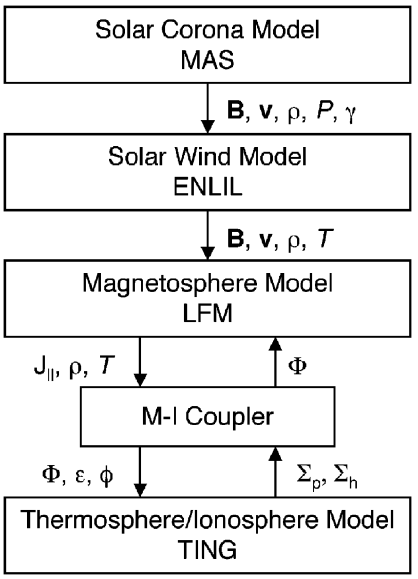

Fig. 1. Schematic overview of the core coupled CISM models: The MAS model of the solar corona, the ENLIL model of solar wind, the LFM model of the magnetosphere, and the TING model of the ionosphere–thermosphere system. Parameters passed between the models: **B**: magnetic field vector; **v**: plasma velocity vector; ρ: plasma density; P: plasma pressure; γ: ratio of specific heats; T: plasma temperature; $J_{\|}$: electric current parallel to **B**; Φ: electric potential field; ε: characteristic energy of precipitating electrons; ϕ: flux of precipitating electrons; Σ_h: Hall conductance; Σ_p: Pederson conductance.

developed by Wang et al. (1999) based on the NCAR thermosphere–ionosphere general circulation model (TIGCM) (Roble et al., 1988). The critical interfaces of the model components include the solar photosphere-corona, the corona-solar wind, the solar wind-magnetosphere, and the magnetosphere–ionosphere–thermosphere. In addition to these core coupled codes and interfaces, there are several important space weather element models that use the results from the MHD codes as a basis for additional computations. These include the rice convection model (RCM) of the inner magnetosphere (Harel et al., 1981; Toffoletto et al., 2003), a kinetic radiation belt code (Hudson et al., 1997), and a solar energetic particle module, which is under development. Here we focus on initial results obtained with the core coupled codes only (corona, solar wind, magnetosphere, and thermosphere/ionosphere), without the inner magnetosphere and particle models. Details of the computational methods used in coupling the core CISM models are described in accompanying papers (e.g., Odstrcil et al., this issue; Wiltberger et al., this issue; Goodrich et al., this issue).

For the first example of a simulated Sun-to-upper atmosphere space weather event using the CISM approach we chose the case of an ad hoc transient similar to a coronal mass ejection (CME) initiated at the Sun by magnetic flux cancellation at the photospheric boundary (Linker et al., 2003). This scheme self-consistently produces a coronal and interplanetary magnetic flux rope with simulated coronagraph white-light images resembling observations, and in situ parameters at 1 AU resembling observed magnetic clouds. Parameters at a point near the center of the passing interplanetary coronal mass ejection (ICME) are used to drive the coupled magnetosphere–ionosphere–thermosphere models. The test case is found to produce geomagnetic and upper atmosphere responses similar to those during a magnetic storm. The results provide initial insights into the consequences of using a modular, coupled, physically complex model of space weather, and suggest how such models can incorporate observations for both boundary condition specification and parameterizations of additional physical processes.

2. Description of models

2.1. Corona and heliosphere model description

A number of earlier papers describe the corona and solar wind simulations used by CISM in both separate and coupled forms (e.g., Mikic et al., 1999; Odstrcil et al., 2002a, b; Riley et al., 2002; Linker et al., 2003). To briefly summarize their attributes: The MAS 3D MHD model of the solar corona is based on a polytropic equation of state, with a ratio of specific heats γ of 1.05

used to approximate coronal thermodynamical properties and consequences. A finite resistivity and viscosity are included, consistent with the expected effects of coronal processes. The spherical computational grid, illustrated in Fig. 2a, extends from the photosphere to its outer boundary at 30 solar radii. The cell spacing is graduated in both the radial and latitudinal dimensions, allowing concentration of higher spatial resolution along a predetermined latitude plane of interest, such as the equator. Simulations are initiated with a potential (current free) description of the coronal magnetic field based on a global photospheric field map either created or derived from magnetograph observations. A uniform boundary density and Parker-type solar wind outflow completes the specification of initial conditions.

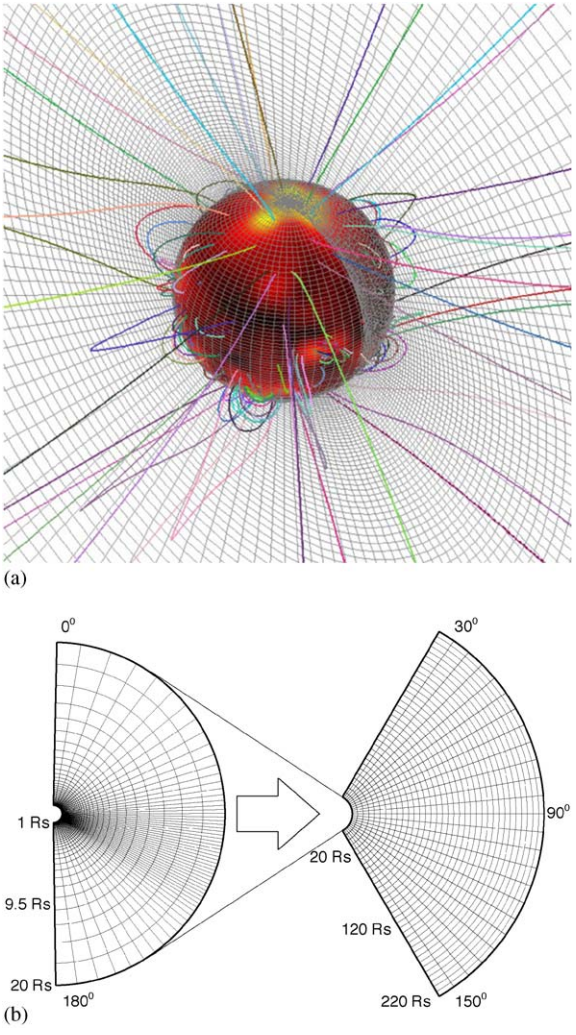

Fig. 2. (a) Illustration of the spherical computational grid of the MAS model. (b) The relative properties and scales of the MAS and ENLIL grids illustrated by a meridional section.

Like other steady state MHD descriptions of the corona (e.g., Usmanov, 1993), the MAS simulation produces coronal magnetic fields with both magnetically closed regions, where coronal density is highest, and open field regions of relatively low density that channel outflowing coronal plasma or solar wind. The large-scale closed fields encircle the Sun with a toroidal arcade of field lines, the helmet streamer belt or arcade. Coronagraph observations have long suggested that this structure is involved in coronal transient activity (Hundhausen, 1991). The helmet streamer arcade is bounded on the outside by the last closed field lines of the corona, whose highest points are cusps at a few solar radii marking the base of the heliospheric current sheet. These cusps and their extensions are also observable in coronagraph images as coronal streamers. The open field regions of the corona are often called coronal holes because of their typical dark appearance in solar XUV images.

MAS coronal simulations have been shown to reproduce the coronal streamer geometries observed in eclipse and coronagraph pictures when observed photospheric field synoptic maps are used to describe their inner boundary conditions (Mikic and Linker, 1996). However, while the solar wind produced in this polytropic coronal model has the desirable behavior, suggested by observations, of a speed gradient at the boundary of open and closed field lines (e.g., Linker et al., 1999), its highest speeds are too low by roughly a factor of two to three and the speed contrasts are weaker than inferred from solar wind observations. The outflow speed, as well as the contrast between the low and high speeds, must be increased by use of a more accurate treatment of the energy equation, including introduction of wave heating and momentum deposition terms (Mikic et al., 1999). The MAS model outflow is nevertheless supercritical, or supermagnetosonic, at the outer boundary of the MAS grid at 30 R_S.

Time-dependent photospheric inner boundary conditions are implemented in the MAS code as described by Mikic et al. (1999). In brief, a finite tangential electric field is imposed consistent with the time derivative of the boundary magnetic field. The flows implied by this electric field can result in important changes such as flux cancellation at a magnetic neutral line, thought to be a key element of coronal eruptions. For general evolving magnetic field boundary conditions, the modeled coronal fields open and close with time, producing transient structures with a variety of properties and geometries.

The initial ambient solar wind and coronal transients in the outer grid layers of the MAS model are used to drive the inner boundary of the ENLIL solar wind simulation. ENLIL is a 3D ideal MHD model (Odstrcil et al., 2002b) designed to treat supercritical outflows in the limit where resistivity and viscosity are minimal. Like the MAS code, it is based on a polytropic equation

of state, but in this case a value of $\gamma = 1.5$ is used, based on interplanetary observations (Totten et al., 1995). For the study described here, the ENLIL model domain extends from the solar equator to within 30° of both poles. This concentrates the uniform latitude-longitude spherical grid on the region of heliospace influencing Earth, while allowing sufficient latitudinal range to minimize the effects of neglecting high latitude behavior. The relative properties of the MAS and ENLIL grids are illustrated by the meridional slices shown in Fig. 2b (Odstrcil et al., 2002a). The "guard cell" method for coupling the solutions of the MAS code to the ENLIL code, as well as the handling of the γ and time step differences, are described in detail in an accompanying paper by Odstrcil et al. (this issue).

Solar rotation is introduced at the MAS/ENLIL model interface by advancing the coronal model parameters in longitude by the appropriate amount at each solar wind model time step. The result is the appearance of a Parker spiral interplanetary magnetic field geometry and weak solar wind stream interaction features in which spiral density ridges and rarefaction regions are formed (e.g., Pizzo, 1991). This geometry also gives rise to the 3D "ballerina skirt" heliospheric current sheet (Riley et al., 2001), with the spiral magnetic field directions on either side outward or inward depending on the polarity of the solar field in its coronal open field source regions.

In the coupled solar-heliospheric CME simulation described below, the values at the outer boundary of the MAS simulation are passed directly to ENLIL without modification. The coupled models can also be used to produce global quasi-steady models of the corona and inner heliosphere. In that case, because the contrast in solar wind speed in the coronal simulations is typically 10–30% rather than the observed factor of ~2, the solar wind speed at the MAS-ENLIL interface is adjusted to a more realistic range of ~400–600 km/s by applying an open field geometry-dependent correction factor (Riley et al., 2001). ENLIL has also been run for ambient solar wind simulations using the empirical Wang–Sheeley–Arge coronal model (Odstrcil et al., 2002b; Arge et al., this issue) in place of the MAS coronal code driver, in an early demonstration of the modularity of the CISM heliospace model.

2.2. Magnetosphere–ionosphere–thermosphere model description

The global configuration of the magnetosphere is calculated using the LFM model (Fedder and Lyon, 1995; Fedder et al., 1995; Lyon et al., this issue). The LFM model solves the ideal MHD equations on a non-uniform grid containing the magnetosphere, magnetosheath, and surrounding solar wind, that ranges from 30 Earth radii (R_E) upstream to 300 R_E downstream, and has a lateral dimension of 100 R_E. Fig. 3a shows a schematic of the LFM numerical grid. The outer boundary conditions applied to the front and sides of this nearly-cylindrical domain are the supersonic flow conditions of the solar wind plasma, i.e., its density, temperature and velocity, and the interplanetary magnetic field vector. In the absence of high-resolution information concerning the small-scale variability of solar wind and IMF parameters, these are generally taken to be constant across planar fronts flowing from upstream into the model grid, i.e., in the y–z plane in geocentric solar magnetic (GSM) coordinates. In situ measurements such as from the ACE or WIND spacecraft can provide time-dependent measurements of the heliospheric conditions upstream of the magnetosphere and are often used as model boundary conditions. Alternatively, solar wind conditions can be obtained from idealized constraints, semi-empirical models, or heliospheric models. In this study, the latter approach is employed, in order to couple the magnetospheric response to the MAS/ENLIL description of the heliospheric drivers.

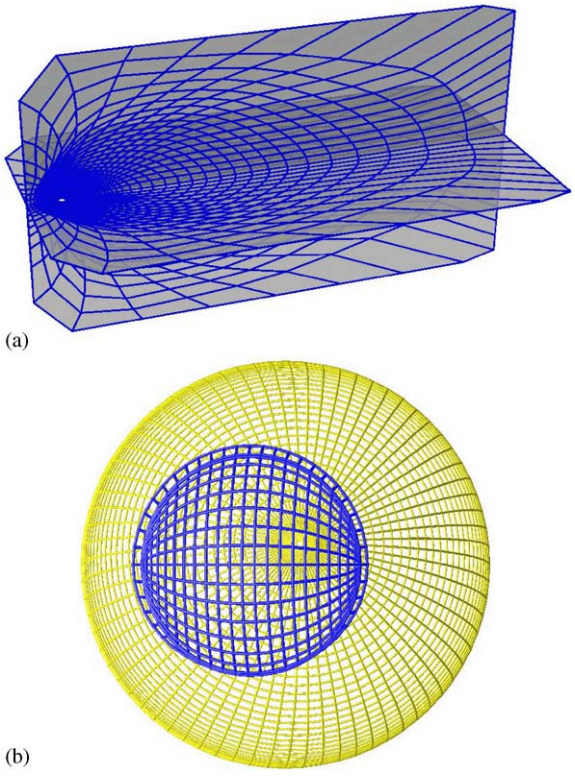

Fig. 3. (a) Illustration of the LFM computational grid. (b) Overlay of the rotating geocentric equatorial TING grid (yellow) and solar-magnetic LFM grid (blue) in the polar region.

The LFM model has been shown to reproduce some of the important magnetospheric responses to interplanetary clouds such as the January 6–10, 1997 ISTP event (Goodrich et al., 1998). Magnetospheric instabilities such as substorms have also been studied with the LFM model (Lyon et al., 1998; Pulkkinen et al., 1998; Wiltberger et al., 2000). Although substorms are not the focus of the present study, they occur together with magnetic storms and are thus a part of the physical response of the magnetosphere to interplanetary conditions. The amount of southward compressed field in the sheath and ejecta of the ICME, together with the order and duration of northward and southward fields in both, dictates important magnetospheric responses such as when (or if) a magnetotail plasmoid is ejected and when a ring current would be injected. However, ring current physics are not yet included in the LFM model. Work is in progress (Toffoletto et al., this issue) to couple the RCM of the inner magnetosphere to the LFM model, and ultimately to a plasmasphere model as well. In the interim, the rudimentary ring current present in the LFM simulation from the redirection of existing plasma flows gives a rough idea of the timing of an injection for a specific set of interplanetary conditions. As found in observations, the ring current injection peaks during the ICME period of largest, most sustained southward upstream magnetic fields, which can occur either in the ICME sheath and/or the following ejecta (e.g. Li and Luhmann, 2004).

The computational inner boundary of the domain is a sphere of radius 2 to 3 R_E. When the LFM model is used as a "stand alone" model, this boundary is coupled to a simplified 2D model of the high latitude ionosphere, which provides the electric field boundary condition for the sphere at the interior of the MHD domain. The ionospheric electric field is calculated using a series of semi-empirical relationships between the field-aligned currents, auroral electron number flux and characteristic energy, and ionospheric conductance. A detailed description of this process is provided by Wiltberger et al. (this issue). The 2D ionosphere approach includes the parameterized effect of solar radiation on the spatial distribution of conductance, but it cannot include the effects of altitude variation of composition, thermospheric neutral winds, rotation of the atmosphere, or global ionospheric electrodynamics, nor can it describe the effects of solar-driven events on the upper atmosphere. Since ionospheric conductance is a crucial element in the feedback from the ionosphere to the magnetosphere (c.f., Raeder et al., 2001; Ridley et al., 2003), it is the goal of this work to couple the LFM model to sophisticated general circulation models of the ionosphere-thermosphere system, and ultimately to the plasmasphere and middle-atmosphere as well.

A series of theoretical models describing the upper atmosphere and ionosphere have been developed over three decades by R.G. Roble and collaborators at the National Center for Atmospheric Research (NCAR). This evolution began with the thermospheric general circulation model (TGCM) (Dickinson et al., 1981), added a coupled ionosphere in the T*I*GCM (Roble et al., 1988), included fully-interactive ionospheric electrodynamics in the TI*E*-GCM (Richmond et al., 1992) and the mesosphere in the TI*M*E-GCM (Roble and Ridley, 1994). A version that included the capability for high-resolution nested-grid computation was developed using the TIGCM as its base by Wang et al. (1999). This, the TING model, is currently employed for two-way coupling simulations with the LFM model.

The TING model solves the time-dependent momentum, energy, and continuity equations on a 3D geographic domain at a resolution of 5° in latitude and longitude. Its high-resolution nested-grid capability is not employed for the model coupling studies described here. The pressure-level grid extends from an equivalent altitude of about 97 km to approximately 500 to 700 km, depending on solar activity, at a resolution of two levels per scale height. A dynamically-coupled ionosphere is calculated considering that transport is significant for O^+ but that the other major ion species are in local chemical equilibrium, and assuming that the electron density is equal to the sum of the ion densities. The inputs driving the model are solar ultraviolet and X-ray radiation at the top of the atmosphere, the electric field and auroral precipitation pattern imposed by the magnetosphere on the upper boundary in the polar regions, and the pressure changes due to atmospheric tides applied to the lower boundary. A more detailed description is given by Wang et al. (this issue).

Two-way coupling between the LFM and TING models is accomplished using a method similar to the procedure employed by the LFM model in coupling to its simplified ionosphere, described above and by Wiltberger et al. (this issue). Solar wind and IMF parameters drive the LFM external boundary conditions at a 60 s cadence and the MHD equations are solved using a variable time-step with typical duration of 0.25 s. Once per every 120 s, auroral electron number flux and characteristic energy are calculated from the field-aligned currents at the inner boundary, using the same empirical relationships between currents and particle flux parameters that are employed in the "stand alone" LFM model. These auroral electron fluxes are interpolated onto a rotating geocentric equatorial grid (Fig. 3b) and applied to the upper boundary of the TING model. TING then performs a single 120 s time-step, calculating the conductivity at every grid point and at every pressure level using the ion and neutral densities obtained, and vertically integrating to produce the conductance pattern. The LFM model is then run for another ~480 time-steps using that conductance distribution as its inner boundary before another TING

time-step is performed. Thus, the magnetosphere calculation lags the conductance calculation by up to 2 min. This has some physical justification, since the ion density calculation assumes immediate convergence to chemical equilibrium given the auroral flux parameters, but this process actually has a time constant on the order of 10–100 s, depending on electron density and altitude. Neutral wind effects on the electric field potential pattern caused by collisions with ions, including the Earth rotation component, are not yet included in feedback to the magnetosphere.

From the thermospheric point of view, the LFM specification of auroral parameters replaces the empirical or climatological inputs otherwise used at auroral latitudes to specify the electric field and particle precipitation. Quantification of the differing effects on thermospheric circulation and heating when using coupled MHD calculations instead of empirical-climatological specifications is of crucial importance; Wang et al. (this issue) describe initial efforts in this area.

3. Event simulation

3.1. Corona and heliosphere simulation

The objective of this case study is to produce a three-dimensional disconnected coronal structure within the helmet streamer arcade with the magnetic topology of a flux rope over a limited range of solar longitude. Moreover, this structure must erupt in a reasonable amount of model run time. The details of the simulation are described by Linker et al. (2003); here we briefly describe some key features. The initial state is a helmet streamer configuration, formed from a photospheric field that combines a dipolar field with a more concentrated bipolar flux distribution. The distribution is azimuthally symmetric but is not symmetric in latitude, with the magnetic equator occurring at 17° south latitude. The solar wind speed near the poles in the simulated streamer is 385 km/s near 30 R_S, while that near the equator is 330 km/s. The magnetic field in the streamer is highly sheared, as is typically observed in solar filaments (Martin and Echols, 1994). The flux cancellation process is modeled by the slow reduction of photospheric flux over a 180° longitudinal extent of the helmet streamer, resulting in the formation of a 3D stable flux rope configuration with ends anchored in the photosphere. Further flux reduction results in magnetic destabilization of the configuration, ejecting both the flux rope and a portion of the streamer belt into the outer corona. Its progress with time is illustrated by a sequence of snapshots of selected coronal magnetic field lines in Fig. 4. This figure also shows polarization brightness images constructed from the simulation as if the eruption were viewed on the limb, slightly inclined from the equator. As noted by Linker et al., these exhibit the classical three-part CME structure of a bright core inside a dark cavity with an overlying bright loop. In the present case study the ejecta are centered on the Sun–Earth line instead of at 90° to it. The simulated CME drives into the slow solar wind ahead of it, and is traveling at >500 km/s when it exits the coronal simulation domain.

The plasma and magnetic fields from the MAS simulation are supplied as the lower boundary condition for the ENLIL code as described by Odstrcil et al. (2002a). A steady-state solar wind is established by numerical relaxation in the heliospheric domain prior to the initiation of the simulated CME. The ejecta reach the outer boundary of the corona model and enter the domain of the heliospheric calculation about 10 hours after the eruption begins to leave the Sun. Odstrcil et al. (2002b) describe the 3D evolving coronal transient, which includes a clearly distinguishable sheath portion of heated, compressed solar wind between the leading shock and the ejected flux rope. The shape and progression of the shock, together with the sheath and flux rope contributions to the following geo-effective structure, are illustrated in Fig. 5. Behind the moving shock, identified by its density jump (Fig. 5a), the ambient interplanetary field is compressed and deflected out of the plane containing the moving flux rope, producing a north–south interplanetary field component of enhanced magnitude (Fig. 5b). The ejecta fields (Fig. 5c) exhibit a subsequent rotating north–south component or bipolar signature as viewed by a stationary observer.

Fig. 6 shows the progression of the simulated ICME shock parameters (density jump, shock speed, and Mach number) along the Sun–Earth line for the study event. These are derived at the surface defining the midpoint of the shock-related momentum jump from the upstream and downstream values. The shock forms at ~0.2–0.3 AU from steepening of compressional pressure waves that starts in the corona at the leading edge of the ejected flux rope, and decelerates beyond ~0.6 AU. Note that the Sun–Earth line skims the edge of the undisturbed slow and dense heliospheric streamer belt. The simulated time series of the standard interplanetary plasma and field parameters of this event, sampled at 1 AU and at the solar equator in the plane through the ejecta central longitude, is shown in Fig. 7. Standard GSM coordinates are used to describe the local interplanetary field orientation. This represents the event as it would be measured at the Earth's upstream libration (L1) point where interplanetary monitoring spacecraft are located.

The MHD simulated event signature includes all of the key parameters of observed ICMEs, except in this case with physically specified and controllable causes and effects. In particular, the north–south magnetic field

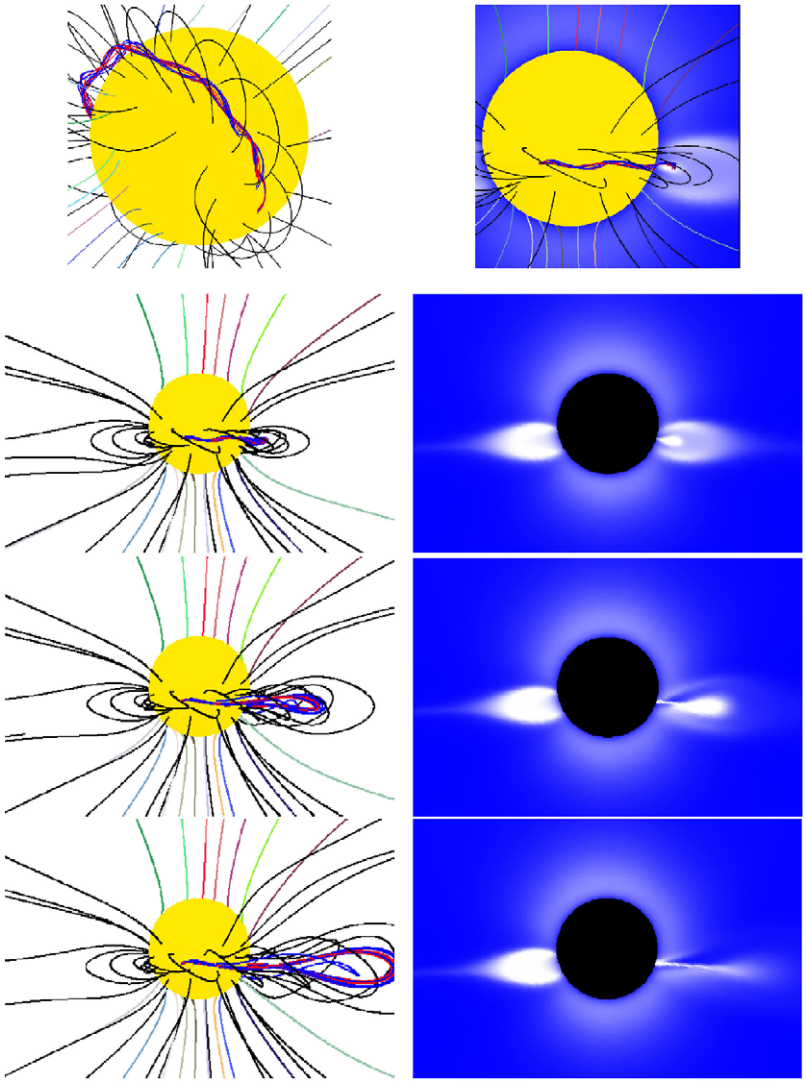

Fig. 4. 3D MHD simulation of a CME triggered by emerging flux. Top: emergence of opposite polarity flux leads to formation of a stable flux rope. Bottom: Further emergence causing eruption is illustrated by a sequence of snapshots of selected coronal magnetic field lines. Scattered white light coronagraph images constructed from the simulation as if the eruption were viewed on the limb are also shown.

component sign or polarity in both the sheath and ejecta structures are determined by the global-scale photospheric field. Experiments with the 1 AU sampling location with respect to the coronal event location and orientation (e.g. Ridley et al., 2003) are straightforward to implement within this code framework. Additionally, the simulated L1 results contain three-dimensional information concerning gradients in the solar wind as it approaches 1 AU, which eventually can be incorporated in the coupling to geospace models.

A recent paper by Manchester et al. (2004) describes a contrasting approach to ad hoc CME initiation and transport. Their CME is initiated by introducing an analytical MHD model of a stretched toroidal flux rope (Gibson and Low, 1998) within the closed fields of the equatorial helmet streamer belt. Its primary driving force is the magnetic pressure within the flux rope structure, which expands into the ambient solar wind, forming a leading shock. As the rooted structure expands outward, reconnection occurs in its wake due to numerical resistivity. This approach differs from ours in that the structure is not longitudinally extended. It accelerates rapidly to over ~1000 km/s in the low corona, whereas the behavior of our structure is more

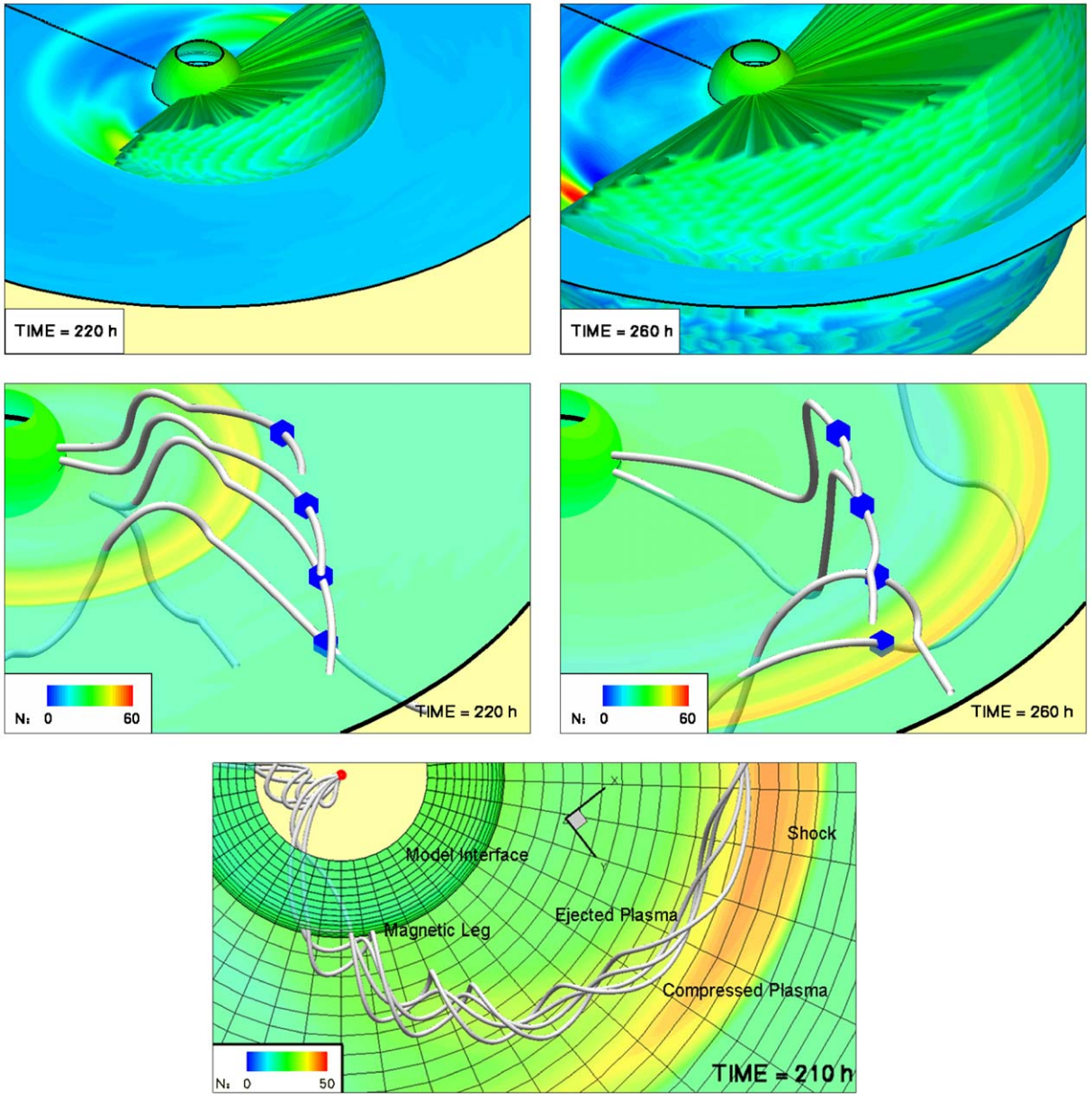

Fig. 5. The shape and progression of an evolving coronal transient simulated by the ENLIL model. Top: The shock, identified by its density jump. Middle: The ambient interplanetary field compressed and deflected out of the plane containing the moving flux rope, producing a north–south interplanetary field component of enhanced magnitude. Plasma density in cm^{-3} are also shown by the color scale. Bottom: The ejecta fields, exhibiting a subsequent rotating north–south component as viewed by a stationary observer.

representative of a typical slow CME (see Fig. 6). Their CME decelerates to ~450 km/s by the time it reaches 1 AU, while ours accelerates to approximately the same speed with minor subsequent change in velocity. Both ejecta structures develop flattened, lenticular meridional cross-sections as they propagate. Other than the opposite polarity, the most notable distinction between the two simulations at 1 AU is the larger density enhancement in our result, and the lower than ambient density in the Manchester et al. (2004) result. (ICME ejecta at 1 AU typically exhibit close to average ambient densities (Gosling et al., 1987).) Considering the great differences in the initiation schemes, the simulated L1 time series are remarkably similar.

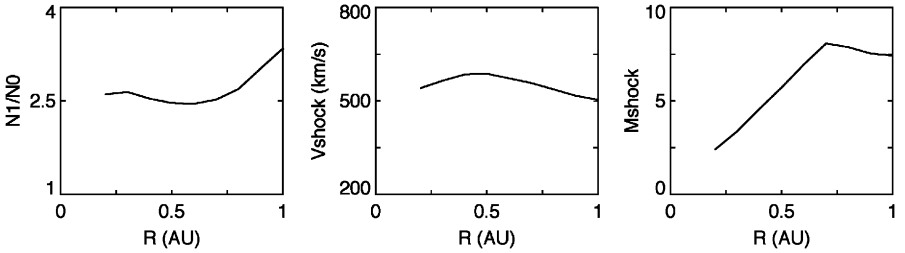

Fig. 6. Shock parameters along the Sun–Earth line, derived from the midpoint of the values upstream and downstream of the shock. Left: density jump. Center: Shock speed. Right: Mach number.

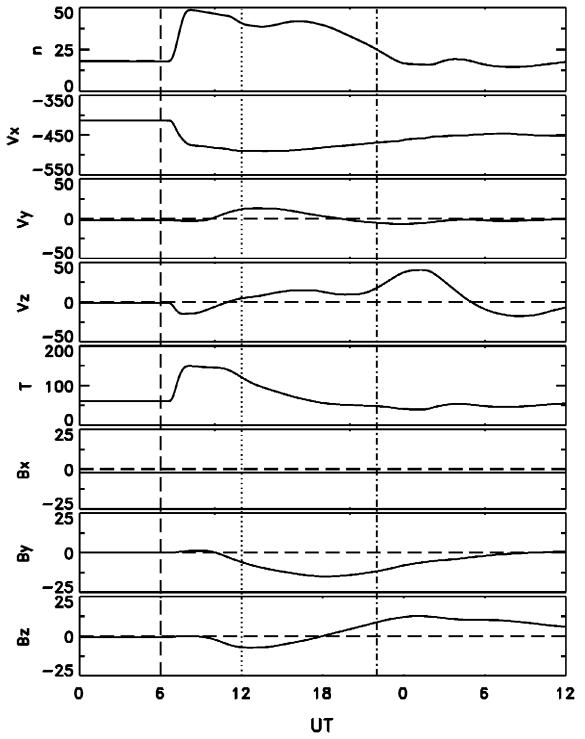

Fig. 7. Simulated time series of the solar wind and interplanetary magnetic field as sampled upstream of the Earth at L1. Top to bottom: Plasma density, cm^{-3}; x, y, and z components of the velocity, km/s; plasma temperature, K; x, y, and z components of the IMF, nT. The vertical dashed lines represent the times of the model output shown in Figs. 8 and 9.

3.2. Magnetosphere–ionosphere–thermosphere simulation

In this initial case study, the simplest interface between the heliosphere and geospace models is employed: The simulated time series of solar wind and IMF parameters at L1 replaces in situ measurements by spacecraft sensors as the upstream boundary condition of the LFM model. These model data are shown in Fig. 7 for a 36-h period at the vernal equinox. Solar minimum conditions are assumed for ultraviolet and X-ray flux values. The sequence is assumed to start at 0 UT. A shock front arrives at 7–8 UT, followed by a magnetic cloud with very enhanced plasma density values of 30–50 cm^{-3}. A modest enhancement and southward turning of the upstream interplanetary magnetic field (IMF) then occurs, reaching a peak negative B_z near 12 UT, then rotates into a period of significantly negative B_y, followed by an extensive period with B_z northward.

The LFM/TING model simulation of the magnetospheric response to these events is shown in Fig. 8, at three times corresponding to the vertical dashed lines on Fig. 7. Plasma density is shown with the "last closed field line" surface superimposed and an inset of the northern auroral region ionospheric conductance computed by the TING model. At 6 UT, just prior to the shock front arrival, the extremely long magnetotail is a consequence of the low IMF values, and the auroral region is faint. By 12 UT, near the peak of the storm, the upstream magnetopause is compressed to 5 R_E, and the tail has retracted to a neutral line near 40 R_E, causing strong reconnection and convection. The polar cap and auroral oval have expanded considerably, and intense precipitation has dramatically increased the conductances. At 22 UT, B_z is northward, but the large negative B_y results in significant ongoing reconnection as the magnetotail begins its recovery.

In Fig. 9, a more detailed view of the ionospheric and thermospheric effects is shown at the same three model times. The left-hand column shows the electron density at the −4 pressure level (~120 km, the E-region) as color contours with the ion drift pattern superimposed. The right hand column gives the neutral temperature distribution at the +2 pressure level (~250 km, the F-region) with neutral wind vectors overplotted. The three rows correspond to 6, 12, and 22 UT. Before the shock impact, because of the slight southward B_z, there is some auroral ionization manifested as enhanced electron densities in the oval, and modest convection. The electron density enhancement in the upper part of

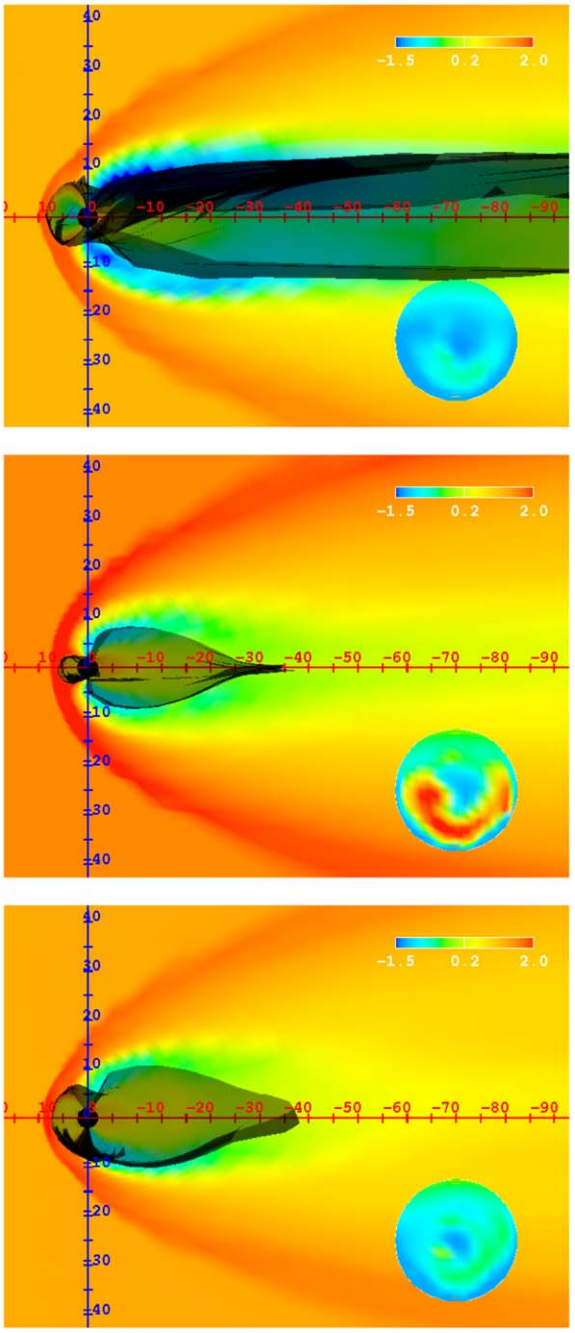

Fig. 8. Configuration of the magnetosphere at 6, 12, and 22 UT as simulated by the LFM/TING coupled model. Plasma density ($\log_{10}$ cm^{-3}) is plotted as a color image with the "last closed field line" surface superimposed. Inset: polar ionospheric conductance morphology as calculated by the TING model.

the plot is due to solar ionization. Neutral winds in the *F*-region are likewise modest, with significant anti-sunward flow caused by a combination of auroral convection and solar-heating driven pressure gradient. At 12 UT, large auroral enhancement of ionization and convection is seen, with a strong two-cell ion convection pattern and response of anti-sunward neutral winds and return flow in the dusk cell. The dawn cell continues to be suppressed, however, due to the effect of coriolis force on cyclonic circulation (Killeen and Roble, 1984). The *F*-region has started to warm, but neutral temperatures are not significantly enhanced until later in the storm, as seen in the plot for 22 UT. Here, a classic negative B_y pattern appears, with continued strong precipitation in a smaller auroral oval, a very small dusk ion convection cell, and little sunward convection in the neutral wind. The temperature continues to increase with complex spatial dependence, including the effect of adiabatic cooling in mid-latitude cold spots. The lower electron densities in the polar cap cause de-coupling of the ion and neutral motions.

Fig. 10 is a plot of the Joule heating distribution in latitude and altitude at 12 UT along a meridian at 0° longitude. The pattern has significant complexity along the equatorward boundary of the auroral oval due to the interplay of ion convection, neutral wind, and ion density, since it is the relative motion of the ions with respect to the neutrals that causes frictional heating. In Fig. 11, a time history of the magnetosphere–ionosphere–thermosphere response to the solar wind forcing is shown using conventional global indices estimated for the northern hemisphere from the model data: The cross-cap potential, integrated hemispheric Joule heating, hemispheric power of precipitating electrons, and the auroral electrojet indices AU and AL. It is notable that even this simple ICME disturbance simulation results in a complex sequence of storm-like geospace events in the coupled models. The simulated auroral indices are typical of a magnetic storm during solar minimum.

4. Discussion

These simulations provide a demonstration of early results from part of the CISM effort. Many complementary activities are proceeding in parallel with the large model coupling and space weather event modeling described above. These include significant efforts in education (Lopez and Hamed, this issue) and in the transfer of knowledge to government and industrial laboratories. The numerical challenges confronting robust coupling of many numerical models, each of which continues to develop its capabilities over time, are also considerable. The results shown here use ad hoc methods to perform effective interim solutions to the computational problems; more sophisticated methodologies planned for future work are discussed by Goodrich et al. (this issue).

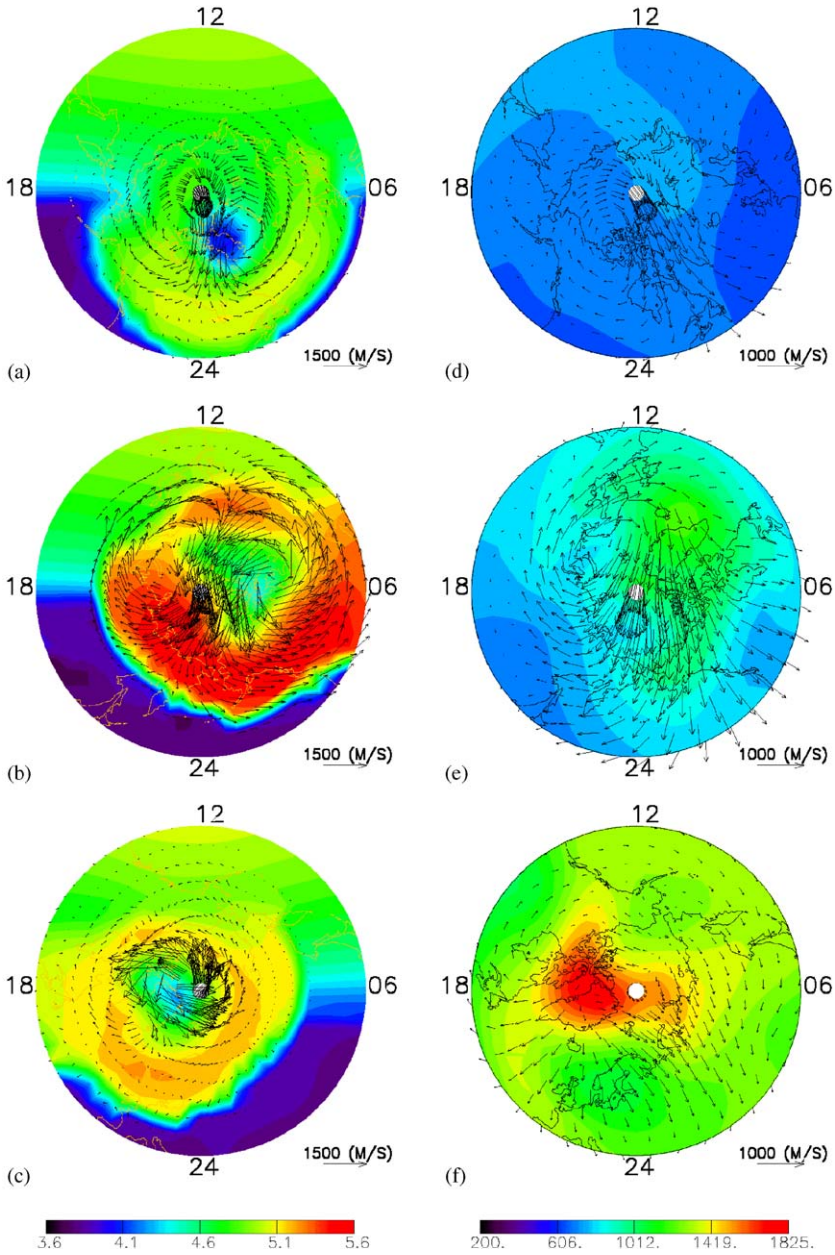

Fig. 9. Response of the thermosphere/ionosphere system calculated by the LFM/TING coupled model at 6, 12, and 22 UT. (a,b,c): E-region electron densities ($\log_{10}$ cm^{-3}) at ~120 km with the ion drift pattern superimposed. (d,e,f): F-region neutral temperatures (K) at ~250 km with the neutral winds superimposed.

It has already been demonstrated that the CISM coupled corona and solar wind models can produce approximations to the ambient solar wind stream structure when photospheric scalar magnetograms are used to specify the coronal field inner boundary conditions (Odstrcil et al., 2002a). The issues of solar wind heating and momentum deposition, described by Mikic et al. (1999), still need to be addressed to bring the velocities and velocity contrasts up to the observed values. As is the case for the empirical solar wind model described by Arge et al. (2003, this issue), MHD solar wind models are useful for driving predictive models of magnetospheric trapped relativistic electrons (e.g., Li et al., 2001) and for

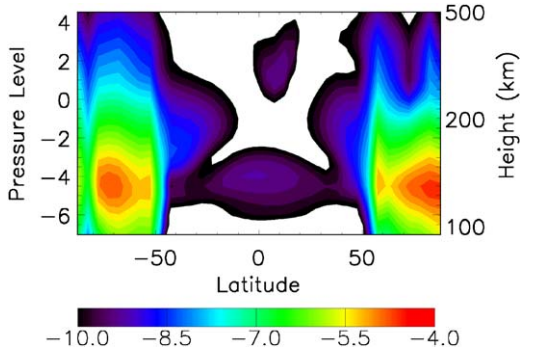

Fig. 10. Joule heating ($\log_{10}$ erg cm^{-3} s^{-1}) calculated by the TING model at 12 UT model time, 0° longitude, as a function of latitude and pressure level (or height).

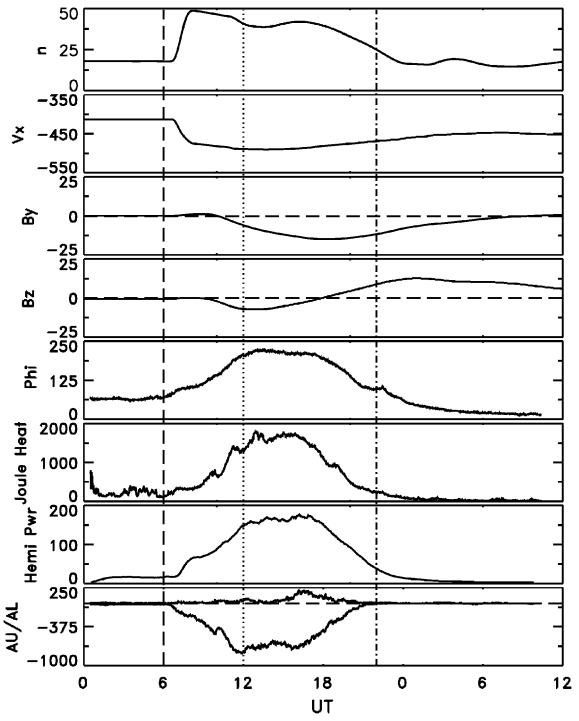

Fig. 11. Parameters representing the global response (northern hemisphere) to the simulated event displayed with a recapitulation of key solar wind parameters at L1. Top to bottom: solar wind density, cm^{-3}; solar wind velocity x-component, km s^{-1}; IMF y and z components, nT; cross-tail potential, kV; hemispheric Joule heating, GW; hemispheric power of precipitating electrons, GW; simulated AU and AL indices, nT. The vertical dashed lines represent the times of the model output shown in Figs. 8 and 9.

predicting the modest recurrent magnetic storms associated with solar wind stream interaction features at 1 AU.

The problem of generating realistic coronal mass ejections which propagate in a solar wind stream context to affect geospace is a critical challenge for the CISM effort. This is also a focus of the parallel multi-university research initiative (MURI) effort led by UC Berkeley Space Sciences Laboratory. Members of these teams are examining the prospects for CME initiation using vector magnetograms, which will soon become more routinely available due to new observational initiatives. Vector magnetograms are thought to contain critical information about stressed lower coronal magnetic field configurations that lead to eruptions. The objective is that magnetograph data eventually be used to simulate the properties of the coronal ejecta as well as their solar wind stream context. Progress toward this goal is described in an accompanying paper (Abbett et al., this issue). Periods of potential case study events, due to their simplicity and the completeness of the observational coverage, are described by Li et al. (this issue).

As noted above, the magnetosphere–thermosphere results shown here are limited by the single-fluid MHD description of magnetospheric morphology and convection. However, the LFM model has been coupled with the RCM inner magnetosphere model in a one-way sense, and work is in progress on two-way coupling (Toffoletto et al., this issue), which will result in a more accurate description of the inner magnetosphere, including the ring current. Radiation belt modeling, employing time-dependent MHD fields, shows promise for understanding transient injections of externally supplied solar energetic ions (Kress et al., 2004; Hudson et al., this issue) as well as the self-consistent accelerations of internal ions (Elkington et al., this issue). For interaction with the ionosphere, the TING model is sufficient at present, but to include a self-consistent description of ionospheric electrodynamics, transition to a high-resolution version of the TIE-GCM will be required. A plasmasphere component for the TIE-GCM will also be developed. Ultimately, more sophisticated models describing the high-latitude coupling of the magnetosphere and ionosphere, including auroral particle acceleration and polar wind transport back to the magnetosphere, will be necessary (Lotko, this issue).

Detailed numerical modeling of the solar-terrestrial system presents broad and difficult challenges. The expression "space weather" implies an analogy with the field of meteorology, but maturity of heliospheric and geospace modeling commensurate with that achieved by tropospheric forecast models is a distant goal. In the interim, it is likely that empirical and semi-empirical methods for attempting to predict changes in the near-Earth space environment and their propagation into the atmosphere will continue to dominate the operational domain (c.f., Siscoe et al., this issue; Baker et al., this issue). As physical models progress, it is vital to have consistent assessment systems in place for exploring

their validity and quantifying their accuracy, both with regard to their empirical predecessors and with regard to differing methodologies and implementations (Spence et al., this issue). The CISM project demonstrates the value of wide interdisciplinary collaboration; we anticipate that the extension of that principle to other groups and other projects will be necessary for continued progress in this emergent field.

Acknowledgements

This material is based upon work supported in part by CISM, which is funded by the STC Program of the National Science Foundation under Agreement Number ATM-0120950. The National Center for Atmospheric Research is supported by the National Science Foundation.

References

Arge, C.N., Odstrcil, D., Pizzo, V.J., Mayer, L., 2003. Improved method for specifying solar wind speed near the Sun. In: Velli, M., Bruno, R., Malara, F. (Eds.), Solar Wind 10. American Institute of Physics, Melville, NY, pp. 190–193.

Dickinson, R.E., Ridley, E.C., Roble, R.G., 1981. A three-dimensional time dependent general circulation model of the thermosphere. Journal of Geophysical Research 86, 1499.

Fedder, J.A., Lyon, J.G., 1995. The Earth's magnetosphere is 165 R_E long: self-consistent currents, convection, magnetospheric structure, and processes for northward interplanetary magnetic field. Journal of Geophysical Research 100, 3623.

Fedder, J.A., Slinker, S.P., Lyon, J.G., Elphinstone, R.D., 1995. Global numerical simulation of the growth phase and the expansion onset for a substorm observed by Viking. Journal of Geophysical Research 100, 19,083.

Gibson, S., Low, B.C., 1998. A time-dependent three-dimensional magnetohydrodynamic model of the coronal mass ejection. Astrophysical Journal 493, 460.

Goodrich, C.C., Wiltberger, M., Lopez, R.E., Papadapoulos, K., Lyon, J.G., 1998. An overview of the impact of the January 10–11, 1997 magnetic cloud on the magnetosphere via global MHD simulations. Geophysical Research Letters 25, 2537.

Gosling, J.T., Baker, D.N., Bame, S.J., Feldman, W.C., Zwickl, R.D., Smith, E.J., 1987. Biderectional solar wind electron heat flux events. Journal of Geophysical Research 92, 8519.

Groth, C.P.T., DeZeeuw, D.L., Gombosi, T.I., Powell, K.G., 2000. Global three-dimensional MHD simulation of a space weather event: CME formation, interplanetary propagation, interaction with the magnetosphere. Journal of Geophysical Research 105, 25053.

Harel, M., Wolf, R.A., Reiff, P.H., Spiro, R.W., Burke, W.J., Rich, F.J., Smiddy, M., 1981. Quantitative simulation of a magnetospheric substorm 1, model logic and overview. Journal of Geophysical Research 86, 2217.

Hudson, K.K., Elkington, S.R., Lyon, J.G., Marchenko, V.A., Roth, I., Temerin, M., Blake, J.B., Gussenhoven, M.S., Wygant, J.R., 1997. Simulation of radiation belt formation during storm sudden commencements. Journal of Geophysical Research 102, 14087.

Hundhausen, A.J., 1991. Sizes and locations of coronal mass ejections: SMM observations from 1980 and 1984–1989. Journal of Geophysical Research 96, 7831.

Killeen, T.L., Roble, R.G., 1984. An analysis of the high-latitude thermospheric wind pattern calculated by a thermospheric general circulation model, 1, momentum forcing. Journal of Geophysical Research 89, 7509.

Kress, B.T., Hudson, M.K., Perry, K.L., Slocum, P.L., 2004. Dynamic modeling of geomagnetic cutoff for the 23–24 November 2001 solar energetic particle event. Geophysical Research Letters 31, L04808.

Li, X., Temerin, M., Baker, D.N., Reeves, G.D., Larson, D., 2001. Quantitative prediction of radiation belt electrons at geostationary orbit based on solar wind measurements. Geophysical Research Letters 28, 1887.

Li, Y., Luhmann, J., 2004. Solar cycle control of the magnetic cloud polarity and the geoeffectiveness. Journal of Atmospheric and Solar Terrestrial Physics 66, 323.

Linker, J., Mikic, Z., Biesecker, D.A., Forsyth, R.J., Gibson, W.E., Lazarus, A.J., Lecinski, A., Riley, P., Szabo, A., Thompson, B.J., 1999. Magnetohydrodynamic modeling of the solar corona during whole sun month. Journal of Geophysical Research 104, 9809.

Linker, J.A., Mikic, Z., Lionello, R., Riley, P., Amari, T., Odstrcil, D., 2003. Flux cancellation and coronal mass ejections. Physics of Plasmas 10, 1971.

Lyon, J.G., Lopez, R.E., Goodrich, C., Wiltberger, M., Papadopoulos, K., 1998. Simulation of the March 9, 1995 substorm: auroral brightening and the onset of lobe reconnection. Geophysical Research Letters 25, 3039.

Manchester, W.B., Gombosi, T., Roussev, I., Ridley, A., DeZeeuw, D.L., Sokolov, I., Powell, K.G., Toth, G., 2004. Modeling a space weather event from the Sun to the Earth: CME generation and interplanetary propagation. Journal of Geophysical Research 109, A02107 doi:2003-JA010150.

Mikic, Z., Linker, J.A., 1996. Large-scale structure of the solar corona and inner heliosphere. In: Winterhalter, D., Gosling, J.T., Habbal, S.R., Kurth, W.S., Neugebauer, M. (Eds.), Solar Wind 8. American Institute of Physics, Melville, NY, p. 104.

Mikic, Z., Linker, J.A., Schnack, D.D., Lionello, R., Tarditi, A., 1999. Magnetohydrodynamic modeling of the global solar corona. Physics of Plasmas 6, 2217.

National Space Weather Program Council, 2000. National Space Weather Program Implementation Plan, 2nd (Ed.). Office of the Federal Coordinator for Meteorology document FCM-P31-2000.

Odstrcil, D., Pizzo, V.J., 1999. Three-dimensional propagation of coronal mass ejections (CMEs) in a structured solar wind flow, 1, CME launched within the streamer belt. Journal of Geophysical Research 104, 483.

Odstrcil, D., Linker, J.A., Lionello, R., Mikic, Z., Riley, P., Pizzo, V.J., Luhmann, J.G., 2002a. Merging of coronal and heliospheric two-dimensional MHD models. Journal of Geophysical Research 107 doi:2002JA009334.

Odstrcil, D.J., Linker, J.A., Lionello, R., Mikic, Z., Riley, P., Pizzo, V.J., Luhmann, J.G., 2002b. 3D MHD simulations of CMEs by coupled coronal and heliospheric models. In: 10th European Solar Physics Meeting, Prague, Czech Republic. ESA, Noordwijk, pp. 95–98.

Pizzo, V.J., 1991. The evolution of corotating stream fronts near the ecliptic plane in the inner solar system, 2, three-dimensional tilted-dipole fronts. Journal of Geophysical Research 96, 5405.

Pulkkinen, T.I., Baker, D.N., Wiltberger, M., Goodrich, C.C., Lopez, R.E., Lyon, J.G., 1998. Pseudobreakup and substorm onset: observations and MHD simulations compared. Journal of Geophysical Research 103, 14847.

Raeder, J., Wang, Y., Fuller-Rowell, T.J., 2001. Geomagnetic storm simulation with a coupled magnetosphere-ionosphere-thermosphere model. In: Song, P., Siscoe, G., Singer, H. (Eds.), Space Weather (AGU Geophys. Monograph 125). American Geophysical Union, Washington DC, p. 377.

Richmond, A.D., Ridley, E.C., Roble, R.G., 1992. A thermosphere/ionosphere general circulation model with coupled electrodynamics. Geophysical Research Letters 19, 601.

Ridley, A.J., Gombosi, T.I., De Zeeuw, D.L., 2003. Ionospheric control of the magnetosphere: Thermospheric neutral winds. Journal of Geophysical Research 108 doi:2002-JA009464.

Riley, P., Linker, J.A., Mikic, Z., 2001. An empirically-driven global MHD model of the solar corona and inner heliosphere. Journal of Geophysical Research 106, 15889.

Riley, P., Linker, J.A., Mikic, Z., Odstrcil, D., Pizzo, V.J., Webb, D.F., 2002. Evidence of post-eruption reconnection associated with coronal mass ejections in the solar wind. Astrophysics Journal Letters 578, 972.

Roble, R.G., Ridley, E.C., 1994. Thermosphere-ionosphere-mesosphere-electrodynamics general circulation model: Equinox solar min simulations. Geophysical Research Letters 21, 417.

Roble, R.G., Ridley, E.C., Richmond, A.D., Dickinson, R.E., 1988. A coupled thermosphere/ionosphere general circulation model. Geophysical Research Letters 15, 1325.

Toffoletto, F., Sazykin, S., Spiro, R., Wolf, R., 2003. Inner magnetospheric modeling with the rice convection model. Space Science Reviews 107, 175.

Totten, T.L., Freeman, J.W., Arya, S., 1995. An empirical determination of the polytropic index for the free-streaming solar wind using HELIOS 1 data. Journal of Geophysical Research 100, 13.

Usmanov, A.V., 1993. A global numerical 3D MHD model of the solar wind. Solar Physics 145, 377.

Wang, W., Killeen, T.L., Burns, A.G., Roble, R.G., 1999. A high resolution, three-dimensional, time dependent, nested grid model of the coupled thermosphere-ionosphere. Journal of Atmospheric and Solar Terrestrial Physics 61, 385.

Wiltberger, M.J., Pulkkinen, T.I., Lyon, J.G., Goodrich, C.C., 2000. MHD simulation of the December 10, 1996 substorm. Journal of Geophysical Research 106, 27649.